Aluminum for Plasmonics
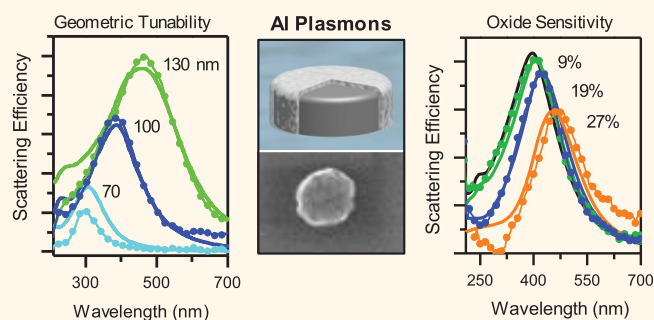
Mark W. Knight,[†,⊥,#] Nicholas S. King,[‡,⊥,#] Lifei Liu,[‡,⊥] Henry O. Everitt,[||] Peter Nordlander,[†,‡,⊥] and Naomi J. Halas[†,‡,§,⊥,*]

[†]Department of Electrical and Computer Engineering, [‡]Department of Physics and Astronomy, [§]Department of Chemistry, and [⊥]Laboratory for Nanophotonics, Rice University, Houston, Texas 77005, United States and [||]Charles Bowden Research Lab, Army Aviation & Missile RD&E Center, Redstone Arsenal, Alabama 35898, United States, and Department of Physics, Duke University, Durham, North Carolina 27708, United States. [#]These authors contributed equally.

ABSTRACT Unlike silver and gold, aluminum has material properties that enable strong plasmon resonances spanning much of the visible region of the spectrum and into the ultraviolet. This extended response, combined with its natural abundance, low cost, and amenability to manufacturing processes, makes aluminum a highly promising material for commercial applications. Fabricating Al-based nanostructures whose optical properties correspond with theoretical predictions, however, can be a challenge. In this work, the Al plasmon resonance is observed to be remarkably sensitive to the presence of oxide within the metal. For Al nanodisks, we observe that the energy of the plasmon resonance is determined by, and serves as an optical reporter of, the percentage of oxide present within the Al. This understanding paves the way toward the use of aluminum as a low-cost plasmonic material with properties and potential applications similar to those of the coinage metals.

RESULTS AND DISCUSSION

Plasmonics is known to hold tremendous potential for transformative applications in optics-based technologies at infrared and optical frequencies. In recent years, there have been significant advances in plasmon-enhanced light harvesting,[1−4] photocatalysis,[5−11] surface-enhanced spectroscopies,[12−16] optics-based sensing,[17−22] nonlinear optics,[23−26] and active optoelectronic applications and devices.[27−31] While plasmons in nanoscale systems can be readily tuned across the visible and into the infrared regions of the spectrum, extending plasmonic properties into the UV has been significantly more challenging because of inherent limitations in the most common plasmonic metals Au and Ag (Figure 1a).[20,32−35] Interband transitions introduce a dissipative channel for Au plasmon resonances at wavelengths shorter than 550 nm; Ag supports resonances down to 350 nm but suffers from rapid oxidation that degrades plasmonic properties. Aluminum has recently been suggested as an alternative plasmonic material in the UV and visible regions of the spectrum.[3,18,36−43] Its attractive properties include low cost, high natural abundance, and ease of processing by a wide variety of methods including CMOS.

To date, however, the experimental optical response of Al nanoparticles has appeared inconsistent relative to calculated spectra, even for well-characterized geometries. Some studies have shown quantitative agreement between experiment and theory, including for high-purity Al nanodisks.[36,39] Other studies, however, have reported discrepancies between experimental and calculated plasmon resonance energies ($\Delta\lambda > 50-100$ nm), especially at ultraviolet energies.[21,37,41] Where discrepancies exist, the experimental resonances are consistently red-shifted relative to values calculated using the tabulated dielectric response of aluminum.

Here we show how the energy of localized surface plasmon resonances depends sensitively on the presence of oxide within the bulk metal. We measure the optical properties of individual Al nanodisks as a function of both measured oxide content and diameter and develop a general approach for modeling their optical response. These results provide a method for estimating the metallic purity of aluminum nanoparticles directly from their optical response.

RESULTS AND DISCUSSION

The plasmonic response of aluminum nanostructures should depend sensitively
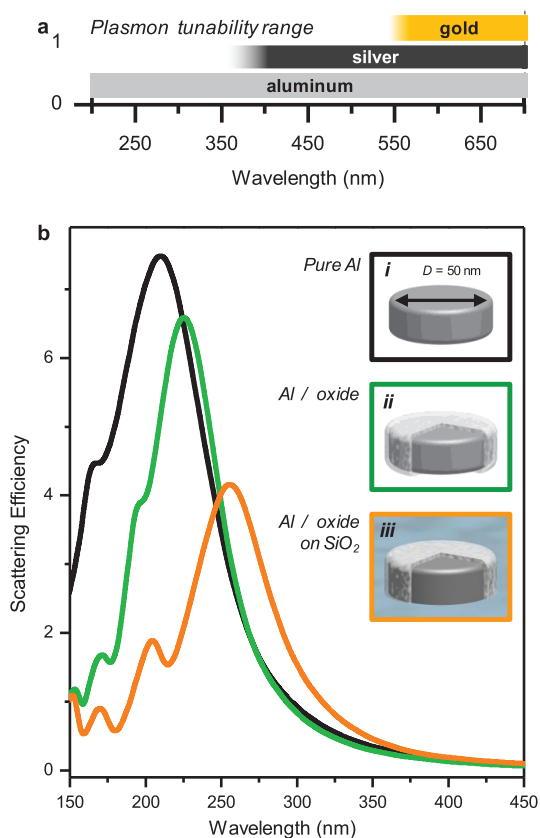
Figure 1. Aluminum as a plasmonic material. (a) Plasmon tuning ranges of the most common plasmonic materials, Au and Ag, compared with Al. **(b)** Calculated spectra for a 35 nm thick, 50 nm diameter Al nanodisk: (*i*) a pure, isolated nanodisk (black line); (*ii*) an isolated Al nanodisk with a 3 nm surface oxide (green); and (*iii*) the same Al nanodisk on an infinite SiO$_2$ substrate (orange).

on both the presence of a surface oxide layer and the presence of a substrate (Figure 1b). For a pure, isolated Al nanodisk with a $D = 50$ nm diameter, the scattering spectrum exhibits a single dipolar resonance at 210 nm (*i*). The addition of a 3 nm surface oxide—a characteristic thickness of the native Al oxide—red shifts the resonance by 15 nm and decreases its amplitude (*ii*). Placed on a dielectric substrate (*e.g.*, SiO$_2$), the nanodisk plasmon resonance red shifts and weakens further, with the dipolar surface plasmon resonance (SPR) shifting to 255 nm and a quadrupolar shoulder appearing as a distinct mode at shorter wavelengths (*iii*).

The spectral response of pure individual Al nanodisks (Figure 2a), fabricated on UV-grade fused silica substrates using e-beam lithography (Figure 2b), was measured as a function of increasing disk diameter using a custom-built hyperspectral UV−visible microscope. For small nanodisks, the deep UV plasmon resonance exhibits the characteristic Lorentzian resonance of a dipolar oscillator. As the nanodisk diameter is increased, phase delay across the nanoparticle causes the plasmon resonance to red shift and broaden and introduces higher order, multipolar resonances. These

experimental spectra remained unchanged when measured following 3 weeks of atmospheric exposure, confirming that the self-terminating native Al oxide very effectively passivates the nanostructures.

Pure Al nanodisk spectra calculated using the finite difference time domain (FDTD) method (Figure 2c) agree well with the experimental dark-field observations. The small geometrical defects in nanodisk geometry apparent in the SEM images (Figure 2b) do not produce significant deviations from the theoretical spectra, which assume perfect disks (Figure 2c). Also, while the excitation conditions are different (see Materials and Methods), the finite numerical aperture of the objective (NA = 0.28) limits the dark-field spectrum to modes that radiate nearly perpendicular to the substrate.[44] This eliminates experimental contributions from out-of-plane plasmonic modes, giving good agreement with the simulated spectra.

Nominally identical Al nanodisks exhibit substantial variations in their plasmon response due to the presence of oxides in the bulk metal (Figure 3). To study this effect systematically, three nanodisk samples were prepared using identical lithographic steps, but with three different deposition chamber conditions: pristine, recently "contaminated", and cleaned following "contamination". First, films were deposited in a dedicated deposition chamber at 10^{-7} Torr. Next, a sample was prepared after contaminating the deposition chamber with a thick layer of SiO$_x$. Aluminum was deposited at 10^{-5} Torr; outgassing from the chamber walls created a partial pressure of oxygen within the chamber. The chamber was subsequently "cleaned" by depositing titanium as a getter and sustaining vacuum levels of $<10^{-5}$ Torr for 1 week. Finally, a third sample was prepared, also at a pressure of 10^{-5} Torr.

The dark-field plasmon response of individual nanodisks fabricated from these films (Figure 3) shows significant spectral effects as a result of the three deposition conditions. For $D = 100$ nanodisks prepared under pristine conditions, the plasmon peak occurs at ∼405 nm (Figure 3a, green points). Immediately following contamination, the plasmon resonance was shifted to 465 nm (orange points), while after cleaning the plasmon shifted back to 417 nm (blue points). Both samples prepared following SiO$_x$ deposition showed a decrease in amplitude of the scattered light relative to nanodisks grown under pristine conditions (green points).

To measure the dielectric response of Al for all three deposition conditions, spectroscopic ellipsometry was performed on smooth films deposited simultaneously with the plasmonic nanodisks for wavelengths between 300 and 700 nm and an incident angle of 70° (Figure 3b). The Al dielectric function for each film was derived from the ellipsometric data assuming a bilayer composed of a thin dielectric Al$_2$O$_3$ layer ($\varepsilon_{ox} = \varepsilon_{Al_2O_3}$)
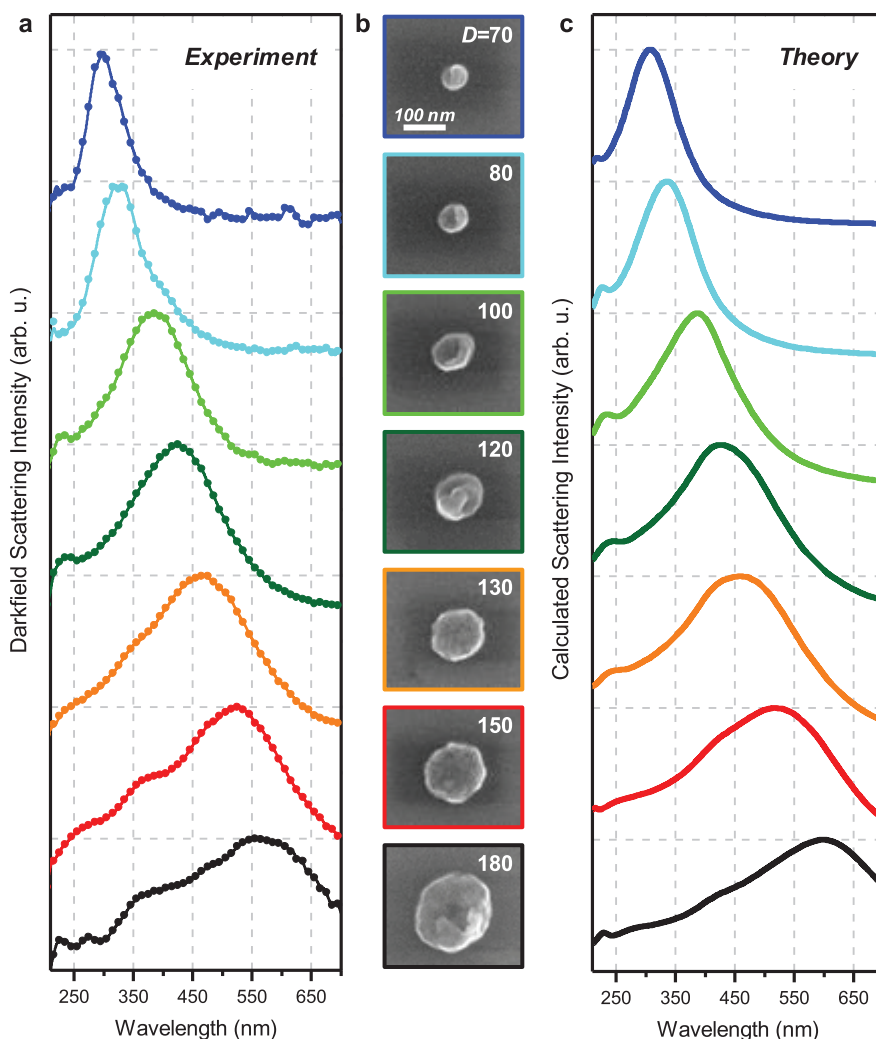
Figure 2. UV−vis tuning of aluminum plasmons. (a) Experimental dark-field spectra of individual nanodisks with D = 70, 80, 100, 120, 130, 150, 180 nm. (b) SEM micrographs of the corresponding nanodisk structures. Scale bar is 100 nm. (c) FDTD simulations of the nanodisk spectra, assuming a 3 nm surface oxide and a SiO_2 substrate.

coating an infinitely thick metallic Al substrate characterized by a modified Drude response (Figure 3b)

$$\varepsilon_{Al} = \varepsilon_\infty - \frac{\omega_p^2}{\omega^2 + i\omega\Gamma} \qquad (1)$$

in which ω_p is the bulk plasmon frequency, Γ is the damping constant, and ε_∞ is the high-frequency response. To within experimental uncertainties, all films exhibited similar surface oxide thicknesses (2−6 nm) and metallic Drude damping ($\Gamma \approx 0.9-1.3$ eV) and ε_∞ (3−4) parameters. However, the bulk plasmon frequency was observed to decrease as trace SiO_x exposure increased, with ω_p = 15.8 eV (green), 14.9 eV (blue), and 12.5 eV (orange).

The observed dependence of the experimental dielectric response on the degree of metal oxidation was modeled as an effective medium composed of oxide inclusions within the host aluminum. The Bruggeman effective medium approximation was found to reproduce the observed behavior more accurately than Maxwell−Garnett theory (see Supporting Information).

The Bruggeman model permits the calculation of a composite Al/Al_2O_3 dielectric function ε by mixing the tabulated values of pure Al and Al_2O_3 as[45,46]

$$n_{Al}\left(\frac{\varepsilon_{Al} - \varepsilon}{\varepsilon_{Al} + 2\varepsilon}\right) + n_{ox}\left(\frac{\varepsilon_{ox} - \varepsilon}{\varepsilon_{ox} + 2\varepsilon}\right) = 0 \qquad (2)$$

where n_{Al} and n_{ox} are the volume fractions of aluminum and oxide comprising the material, respectively. Dielectric functions for the composite metal calculated using this approach (Figure 3c) closely match the experimentally measured permittivities. Slight discrepancies appearing in the imaginary permittivity may arise from either metallic granularity, which varies depending on deposition conditions, or deviations from the Drude model used during ellipsometry to extract the experimental dielectrics.[47]

The Al fractions used to calculate the effective dielectric function for each composite metal film were obtained by fitting the ellipsometrically measured Drude dielectric functions with the Bruggeman dielectric
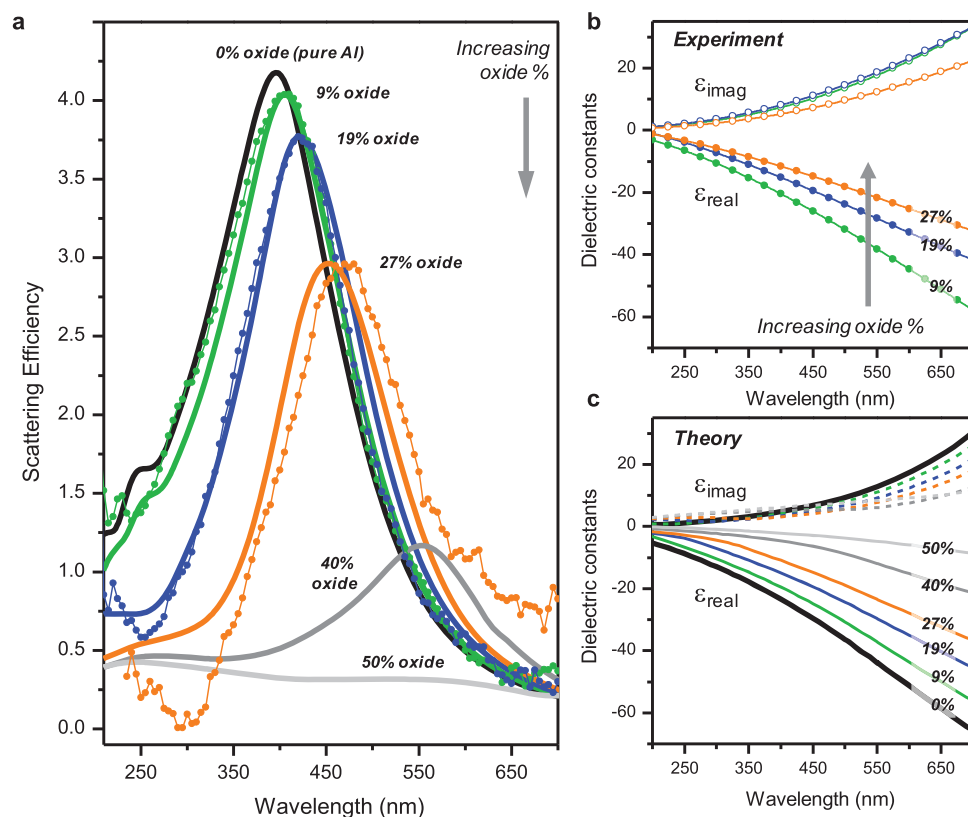
Figure 3. Aluminum dielectric response. (a) Scattering spectra of 100 nm diameter nanodisks with varying metal oxide fractions. The calculated spectra (solid lines) assume a 3 nm pure surface oxide and a SiO_2 substrate. The experimental dark-field spectra (dotted lines, scaled for clarity) correspond to evaporations performed under exposure to varying trace levels of oxygen, producing 9% (green), 19% (blue), and 27% (orange) metal oxide content. (b) Ellipsometrically measured dielectric functions for the three deposited Al purities. (c) Bruggeman dielectric functions for Al oxide fractions of 0% (black), 9% (green), 19% (blue), 27% (orange), 40% (gray), and 50% (light gray).

function, yielding $n_{Al} = 0.91$ (green), 0.81 (blue), and 0.73 (orange). Calculated nanodisk spectra using these composite Al/Al_2O_3 dielectric functions for the core metal and 3 nm of pure Al_2O_3 for the shell agree quite closely with the measured spectra (Figure 3a).

The elemental composition of each film was confirmed under ultrahigh vacuum conditions using X-ray photoelectron spectroscopy (XPS, PHI Quantera). Spectra were acquired for all elements present in the film/substrate system: Al 2p (68–80 eV), O 1s (526–538 eV), C 1s (280–292 eV), and Si 2p (97–109 eV). Using an Al Kα X-ray source, the XPS measurements yielded a response limited to elements present within 10 nm of the exposed sample surface. The elemental composition within the probe volume was obtained from the integrated XPS line shapes after accounting for instrument- and material-dependent relative sensitivity factors. The Al 2p spectrum contains two peaks corresponding to the oxidized and metallic states (75.7 and 73.5 eV).[48,49] Given effective attenuation lengths of $\lambda_{Al} = 2.92$ nm and $\lambda_{ox} = 2.39$ nm, which are specific to Al 2p photoelectron emission,[48] the ratio of the integrated Al and Al_2O_3 peak intensities estimates the relative fractions of oxidized and metallic aluminum within the penetration depth ($\sim3 \lambda_{Al}$) of

the exposed surface. These relative intensities indicate significant differences in oxide content between the three Al samples (Figure 4a).

To determine the compositional depth profile of the film, *in situ* Ar^+ etch cycles (3 kV, 3 × 3 mm area, 12 s increments) and XPS measurements were performed iteratively to estimate the fractional composition just below each freshly exposed surface. Significant aluminum and aluminum oxide peaks were observed (Figure 4a), allowing the depth profile of oxidized Al to be measured quantitatively. In addition, the samples exhibited a minor contribution from carbon—a surface contaminant only observed on the unetched films—and silicon, which only appeared when the etching process had completely removed the 35 nm Al film from the Si substrate and the Al 2p peak had disappeared. Otherwise, the only elements detectable during depth profiling were aluminum and oxygen, with the oxygen appearing in a stoichiometric ratio with aluminum consistent with the measured Al_2O_3. During the first several etch cycles, a rapid decrease in the Al_2O_3 peak was recorded, corresponding to the removal of the passivating surface oxide (Figure 4d). Once the surface oxide layer was removed, the rest of the film exhibited a constant bulk oxide fraction (Figure 4b).
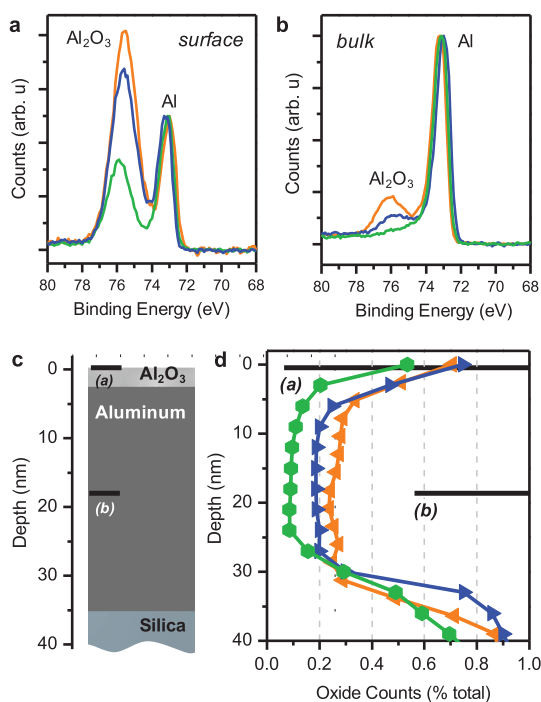
Figure 4. High-purity aluminum deposition. X-ray photoemission spectroscopy (XPS) of the Al 2P peak (73.5 eV) and corresponding oxide peak (75.7 eV) at (a) the surface and (b) within the deposited aluminum film. The films are the same as in Figure 3: 9% (green), 19% (blue), and 27% (orange) metal oxide content. All spectra are normalized to the Al peak for clarity. (c) Schematic drawing denoting scan locations within the film. (d) Fraction of oxidized aluminum within the bulk material is calculated from the relative XPS peak intensities as the film is etched *in situ*, with approximate depths indicated from (c).

For the three different samples, these correspond to unoxidized atomic fractions of 75% (orange), 82% (blue), and 92% (green) Al, in close agreement with the values 73, 81, and 91% Al deduced from ellipsometry and the Bruggeman model. (The XPS counts correspond to atomic fraction, rather than volume fraction, used in the Bruggeman model. Direct application of these data to the Bruggeman model slightly underestimates the oxidized volume, which we estimate to be within our experimental error.) This agreement confirms that Al oxidation beneath the native oxide surface coating occurred *in situ* during deposition from the low levels of trace oxygen present during film growth.

The thickness of the native oxide surface coating may also be estimated from the surface XPS spectrum.[48,49] Approximating the ∼92% Al film as a pure Al substrate of quasi-infinite depth (film thickness >10 λ_{Al}), XPS measurements (Figure 4d, green lines) and appropriate dielectric constants[48] estimate a surface oxide thickness of 3.0 ± 0.1 nm, in close agreement with the native oxide thicknesses measured by ellipsometry and reported in the literature.[39] Indeed, this 3 nm thin native oxide is a ubiquitous and significant characteristic of Al, separate from the deposition-dependent core metal oxidation discussed above.
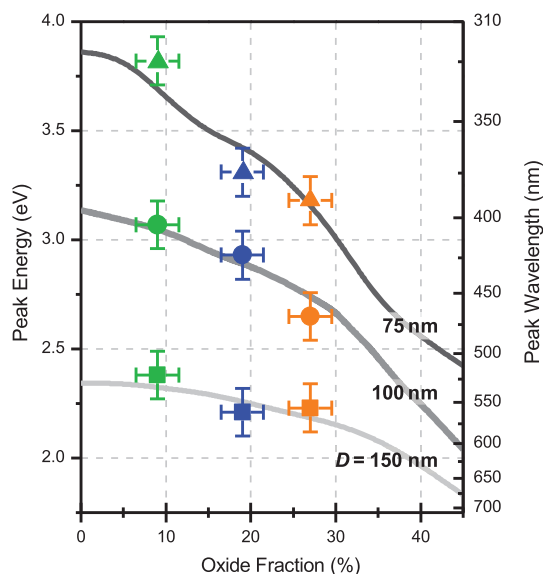

Figure 5. Determining oxide fraction from Al nanodisk scattering spectra. Solid: Calculated plasmon peak energies as a function of core oxide fraction for *D* = 75, 100, and 150 nm nanodisks assuming a 3 nm pure oxide shell. Points: experimentally measured values for 9% (green), 19% (blue), and 27% (orange) oxide content with *D* = 75 nm (triangles), 100 nm (circles), and 150 nm (squares). The error bars indicate typical standard deviations of peak energies for five nominally identical nanodisks (vertical axis) and the maximum difference between the XPS and ellipsometrically measured Al fractions (horizontal axis).

The native oxide strongly affects the plasmonic performance of Al nanodisks because of their high surface-to-volume ratio. For example, the native oxide shell covering a nanodisk with *D* = 100 nm comprises ∼27% of the total nanodisk volume. For smaller nanodisks, this percentage increases rapidly, exceeding 50% for *D* < 27 nm. The total oxide fraction of an Al nanostructure must therefore include both the volume fraction of the native oxide shell and the fractional composition of the composite metal/oxide core.

The close agreement obtained between the experimental and theoretical scattering spectra of the Al nanodisks in Figure 3 reveals that the plasmon energy depends sensitively on the fraction of Al_2O_3 in the core metal. In other words, for Al nanostructures of the same geometry with the same native oxide shell, the core Al_2O_3/Al fraction is a primary determinant of the optical response. These findings indicate that a requirement for reproducible Al-based UV plasmonic nanostructures is fabrication in a pristine environment to minimize the deleterious effects of the bulk metal oxide. Conversely, the optical scattering spectrum of an Al nanodisk can serve as a reporter of Al purity. This is illustrated in Figure 5, where the calculated and measured peak scattering energies for a *D* = 100 nm Al nanodisk are plotted as a function of core oxide fraction. For equivalent nanodisks calculated using the Bruggeman model dielectric function, increasing the core oxide fraction induces a red shift in the dipole

resonance peak from 3.1 eV (400 nm) to 2.0 eV (620 nm) (Figure 5). This reporter functionality is confirmed by the measured resonance energies (Figure 3) for three different nanostructure sizes (Figure 5, circles). Selecting alternate reporter geometries shifts and changes the shape of this calibration curve (see Figure 5, $D = 75$ and 150 nm), suggesting that the smallest diameter nanodisks are the best reporters because their peak energies depend most sensitively on the fraction of bulk oxide present in the nanostructure.

CONCLUSION

We have demonstrated the potential for Al as a high-quality nanoplasmonic material in the UV/visible spectral regions, showcasing the critical importance of Al purity in achieving reproducible plasmonic properties. This requires careful control of oxide contamination during the deposition process. Conversely, an estimation of the oxide fraction may be achieved by matching the spectrum of a known plasmonic nanostructure with spectra calculated using the Bruggeman effective medium approximation. These findings pave the way to develop Al nanostructures for novel UV and visible range plasmonic applications, ultimately enabling high-area, low-cost, CMOS-compatible plasmonic devices and applications not currently possible with noble and coinage metals.

MATERIALS AND METHODS

Theoretical Calculations. Modeling was performed using the finite difference time domain method (FDTD, Lumerical) with nanodisks defined by a diameter D, a thickness of 35 nm, and a 5 nm radius of curvature on all exposed edges. The scattering efficiency, which is the ratio of the scattering cross section to the nanodisk area, was calculated for a normal incidence plane wave, and the optical responses of Al, Al_2O_3, and SiO_2 were specified using tabulated dielectric functions.[46]

Nanodisk Fabrication. Silica substrates were sonicated in acetone for 5 min, rinsed with isopropyl alcohol (IPA), and coated with a 70 nm thick layer of PMMA 950 resist (MicroChem). Following exposure and development (3:1 IPA/MIBK), 99.999% pure Al (Kamis) was deposited using electron-beam evaporation at a rate of ~1 Å/second. All films were 35 nm thick, as measured by a quartz crystal microbalance. Liftoff to expose the nanodisks was performed at room temperature using acetone, followed by an isopropyl alcohol rinse.

Hyperspectral UV Dark-Field Microspectroscopy. The unpolarized output of a continuum light source (Energetiq LDLS) was passed through a monochromator with a 1200 g/mm UV grating to select a narrow frequency band. The output slit of the monochromator was reimaged onto the sample surface using UV-enhanced aluminum mirrors, uniformly illuminating the entire area of interest at an incidence angle of 50°. Scattered light was collected using a 15×, 0.28 NA finite conjugate objective (Edmund Optics, UV ReflX), and imaged onto a UV-enhanced CCD array (Princeton Instruments). Monochromatic images were obtained from 200 to 700 nm in 5 nm increments with a 30 s exposure per wavelength. The images formed a spectral datacube that contained the scattering response of all nanostructures within the field of view, which was then corrected for the instrument response using a UV-grade white calibration standard (Labsphere, Spectralon). All measurements were performed within a dry nitrogen environment to minimize spectral artifacts, with less than 0.3% oxygen (Vernier) and 20 ppb ozone (Ozone Solutions).

Supporting Information Available: Comparison of Al dielectric functions and spectra calculated using both the Bruggeman and Maxwell−Garnett effective medium theories. This material is available free of charge *via* the Internet at http://pubs.acs.org.

REFERENCES AND NOTES

1. Atwater, H. A.; Polman, A. Plasmonics for Improved Photovoltaic Devices. *Nat. Mater.* **2010**, *9*, 205–213.
2. Linic, S.; Christopher, P.; Ingram, D. B. Plasmonic-Metal Nanostructures for Efficient Conversion of Solar to Chemical Energy. *Nat. Mater.* **2011**, *10*, 911–921.
3. Villesen, T. F.; Uhrenfeldt, C.; Johansen, B.; Larsen, A. N. Self-Assembled Al Nanoparticles on Si and Fused Silica, and Their Application for Si Solar Cells. *Nanotechnology* **2013**, *24*, 275606.
4. Villesen, T. F.; Uhrenfeldt, C.; Johansen, B.; Hansen, J. L.; Ulriksen, H. U.; Larsen, A. N. Aluminum Nanoparticles for Plasmon-Improved Coupling of Light Into Silicon. *Nanotechnology* **2012**, *23*, 085202.
5. Mukherjee, S.; Libisch, F.; Large, N.; Neumann, O.; Brown, L. V.; Cheng, J.; Lassiter, J. B.; Carter, E. A.; Nordlander, P.; Halas, N. J. Hot Electrons do the Impossible: Plasmon-Induced Dissociation of H_2 on Au. *Nano Lett.* **2013**, *13*, 240–247.
6. Liu, Z. W.; Hou, W. B.; Pavaskar, P.; Aykol, M.; Cronin, S. B. Plasmon Resonant Enhancement of Photocatalytic Water Splitting under Visible Illumination. *Nano Lett.* **2011**, *11*, 1111–1116.
7. Thomann, I.; Pinaud, B. A.; Chen, Z. B.; Clemens, B. M.; Jaramillo, T. F.; Brongersma, M. L. Plasmon Enhanced Solar-to-Fuel Energy Conversion. *Nano Lett.* **2011**, *11*, 3440–3446.
8. Chen, H. M.; Chen, C. K.; Chen, C. J.; Cheng, L. C.; Wu, P. C.; Cheng, B. H.; Ho, Y. Z.; Tseng, M. L.; Hsu, Y. Y.; Chan, T. S.; *et al.* Plasmon Inducing Effects for Enhanced Photoelectrochemical Water Splitting: X-ray Absorption Approach to Electronic Structures. *ACS Nano* **2012**, *6*, 7362–7372.
9. Warren, S. C.; Thimsen, E. Plasmonic Solar Water Splitting. *Energy Environ. Sci.* **2012**, *5*, 5133–5146.
10. Govorov, A. O.; Zhang, H.; Gun'ko, Y. K. Theory of Photoinjection of Hot Plasmonic Carriers from Metal Nanostructures into Semiconductors and Surface Molecules. *J. Phys. Chem. C* **2013**, *117*, 16616–16631.
11. Mubeen, S.; Lee, J.; Singh, N.; Kramer, S.; Stucky, G. D.; Moskovits, M. An Autonomous Photosynthetic Device in Which All Charge Carriers Derive from Surface Plasmons. *Nat. Nanotechnol.* **2013**, *8*, 247–251.
12. Bochterle, J.; Neubrech, F.; Nagao, T.; Pucci, A. Angstrom-Scale Distance Dependence of Antenna-Enhanced Vibrational Signals. *ACS Nano* **2012**, *6*, 10917–10923.
13. Thomas, R.; Swathi, R. S. Organization of Metal Nanoparticles for Surface-Enhanced Spectroscopy: A Difference in Size Matters. *J. Phys. Chem. C* **2012**, *116*, 21982–21991.

14. Chuntonov, L.; Haran, G. Maximal Raman Optical Activity in Hybrid Single Molecule-Plasmonic Nanostructures with Multiple Dipolar Resonances. *Nano Lett.* **2013**, *13*, 1285–1290.

15. D'Andrea, C.; Bochterle, J.; Toma, A.; Huck, C.; Neubrech, F.; Messina, E.; Fazio, B.; Marago, O. M.; Di Fabrizio, E.; de la Chapelle, M. L.; *et al.* Optical Nanoantennas for Multiband Surface-Enhanced Infrared and Raman Spectroscopy. *ACS Nano* **2013**, *7*, 3522–3531.

16. Zheng, Y. H.; Thai, T.; Reineck, P.; Qiu, L.; Guo, Y. M.; Bach, U. DNA-Directed Self-Assembly of Core-Satellite Plasmonic Nanostructures: A Highly Sensitive and Reproducible Near-IR SERS Sensor. *Adv. Funct. Mater.* **2013**, *23*, 1519–1526.

17. Mattiucci, N.; D'Aguanno, G.; Everitt, H. O.; Foreman, J. V.; Callahan, J. M.; Buncick, M. C.; Bloemer, M. J. Ultraviolet Surface-Enhanced Raman Scattering at the Plasmonic Band Edge of a Metallic Grating. *Opt. Express* **2012**, *20*, 1868–1877.

18. Ono, A.; Kikawada, M.; Akimoto, R.; Inami, W.; Kawata, Y. Fluorescence Enhancement with Deep-Ultraviolet Surface Plasmon Excitation. *Opt. Express* **2013**, *21*, 17447–17453.

19. Jha, S. K.; Ahmed, Z.; Agio, M.; Ekinci, Y.; Löffler, J. F. Deep-UV Surface-Enhanced Resonance Raman Scattering of Adenine on Aluminum Nanoparticle Arrays. *J. Am. Chem. Soc.* **2012**, *134*, 1966–1969.

20. Lal, S.; Link, S.; Halas, N. J. Nano-Optics from Sensing to Waveguiding. *Nat. Photonics* **2007**, *1*, 641–648.

21. Chan, G. H.; Zhao, J.; Schatz, G. C.; Van Duyne, R. P. Localized Surface Plasmon Resonance Spectroscopy of Triangular Aluminum Nanoparticles. *J. Phys. Chem. C* **2008**, *112*, 13958–13963.

22. Chowdhury, M. H.; Ray, K.; Gray, S. K.; Pond, J.; Lakowicz, J. R. Aluminum Nanoparticles as Substrates for Metal-Enhanced Fluorescence in the Ultraviolet for the Label-Free Detection of Biomolecules. *Anal. Chem.* **2009**, *81*, 1397–1403.

23. Castro-Lopez, M.; Brinks, D.; Sapienza, R.; van Hulst, N. F. Aluminum for Nonlinear Plasmonics: Resonance-Driven Polarized Luminescence of Al, Ag, and Au Nanoantennas. *Nano Lett.* **2011**, *11*, 4674–4678.

24. Hentschel, M.; Utikal, T.; Giessen, H.; Lippitz, M. Quantitative Modeling of the Third Harmonic Emission Spectrum of Plasmonic Nanoantennas. *Nano Lett.* **2012**, *12*, 3778–3782.

25. Grubisic, A.; Schweikhard, V.; Baker, T. A.; Nesbitt, D. J. Coherent Multiphoton Photoelectron Emission from Single Au Nanorods: The Critical Role of Plasmonic Electric Near-Field Enhancement. *ACS Nano* **2013**, *7*, 87–99.

26. Walsh, G. F.; Dal Negro, L. Enhanced Second Harmonic Generation by Photonic−Plasmonic Fano-Type Coupling in Nanoplasmonic Arrays. *Nano Lett.* **2013**, *13*, 3111–3117.

27. Knight, M. W.; Sobhani, H.; Nordlander, P.; Halas, N. J. Photodetection with Active Optical Antennas. *Science* **2011**, *332*, 702–704.

28. Konenkamp, R.; Word, R. C.; Fitzgerald, J.; Nadarajah, A.; Saliba, S. Controlled Spatial Switching and Routing of Surface Plasmons in Designed Single-Crystalline Gold Nanostructures. *Appl. Phys. Lett.* **2012**, *101*, 141114.

29. Toroghi, S.; Kik, P. G. Cascaded Plasmonic Metamaterials for Phase-Controlled Enhancement of Nonlinear Absorption and Refraction. *Phys. Rev. B* **2012**, *85*, 045432.

30. Zhang, H. P.; Zhou, J.; Zou, W. B.; He, M. Surface Plasmon Amplification Characteristics of an Active Three-Layer Nanoshell-Based Spaser. *J. Appl. Phys.* **2012**, *112*, 074309.

31. Chen, Y. Y.; Song, G.; Xiao, J. H.; Yu, L.; Zhang, J. S. Subwavelength Polarization Beam Splitter with Controllable Splitting Ratio Based on Surface Plasmon Polaritons. *Opt. Express* **2013**, *21*, 314–321.

32. Khurgin, J. B.; Boltasseva, A. Reflecting upon the Losses in Plasmonics and Metamaterials. *MRS Bull.* **2012**, *37*, 768–779.

33. Naik, G. V.; Shalaev, V. M.; Boltasseva, A. Alternative Plasmonic Materials: Beyond Gold and Silver. *Adv. Mater.* **2013**, *25*, 3264–3294.

34. McMahon, J. M.; Schatz, G. C.; Gray, S. K. Plasmonics in the Ultraviolet with the Poor Metals Al, Ga, In, Sn, Tl, Pb, and Bi. *Phys. Chem. Chem. Phys.* **2013**, *15*, 5415–5423.

35. Yang, Y.; Callahan, J. M.; Kim, T. H.; Brown, A. S.; Everitt, H. O. Ultraviolet Nanoplasmonics: A Demonstration of Surface-Enhanced Raman Spectroscopy, Fluorescence, and Photo-degradation Using Gallium Nanoparticles. *Nano Lett.* **2013**, *13*, 2837–2841.

36. Maidecchi, G.; Gonella, G.; Proietti Zaccaria, R.; Moroni, R.; Anghinolfi, L.; Giglia, A.; Nannarone, S.; Mattera, L.; Dai, H.-L.; Canepa, M.; *et al.* Deep Ultraviolet Plasmon Resonance in Aluminum Nanoparticle Arrays. *ACS Nano* **2013**, *7*, 5834–5841.

37. Ekinci, Y.; Solak, H. H.; Loffler, J. F. Plasmon Resonances of Aluminum Nanoparticles and Nanorods. *J. Appl. Phys.* **2008**, *104*, 083107.

38. Knight, M. W.; Liu, L. F.; Wang, Y. M.; Brown, L.; Mukherjee, S.; King, N. S.; Everitt, H. O.; Nordlander, P.; Halas, N. J. Aluminum Plasmonic Nanoantennas. *Nano Lett.* **2012**, *12*, 6000–6004.

39. Langhammer, C.; Schwind, M.; Kasemo, B.; Zoric, I. Localized Surface Plasmon Resonances in Aluminum Nanodisks. *Nano Lett.* **2008**, *8*, 1461–1471.

40. Taguchi, A.; Saito, Y.; Watanabe, K.; Yijian, S.; Kawata, S. Tailoring Plasmon Resonances in the Deep-Ultraviolet by Size-Tunable Fabrication of Aluminum Nanostructures. *Appl. Phys. Lett.* **2012**, *101*, 081110.

41. Zoric, I.; Zach, M.; Kasemo, B.; Langhammer, C. Gold, Platinum, and Aluminum Nanodisk Plasmons: Material Independence, Subradiance, and Damping Mechanisms. *ACS Nano* **2011**, *5*, 2535–2546.

42. Martin, J.; Proust, J.; Gerard, D.; Plain, J. Localized Surface Plasmon Resonances in the Ultraviolet From Large Scale Nanostructured Aluminum Films. *Opt. Mater. Express* **2013**, *3*, 954–959.

43. Sanz, J. M.; Ortiz, D.; Alcaraz de la Osa, R.; Saiz, J. M.; González, F.; Brown, A. S.; Losurdo, M.; Everitt, H. O.; Moreno, F. UV Plasmonic Behavior of Various Metal Nanoparticles in the Near- and Far-Field Regimes: Geometry and Substrate Effects. *J. Phys. Chem. C* **2013**, *117*, 19606–19615.

44. Knight, M. W.; Fan, J.; Capasso, F.; Halas, N. J. Influence of Excitation and Collection Geometry on the Dark Field Spectra of Individual Plasmonic Nanostructures. *Opt. Express* **2010**, *18*, 2579–2587.

45. Choy, T. C. *Effective Medium Theory: Principles and Applications*; Oxford University Press: Oxford, UK, 1999.

46. Palik, E. D. *Handbook of Optical Constants*; Academic Press: San Diego, CA, 1998.

47. Semaltianos, N. G. Thermally Evaporated Aluminium Thin Films. *Appl. Surf. Sci.* **2001**, *183*, 223–229.

48. Alexander, M. R.; Thompson, G. E.; Zhou, X.; Beamson, G.; Fairley, N. Quantification of Oxide Film Thickness at the Surface of Aluminium Using XPS. *Surf. Interface Anal.* **2002**, *34*, 485–489.

49. Strohmeier, B. R. An ESCA Method for Determining the Oxide Thickness on Aluminum Alloys. *Surf. Interface Anal.* **1990**, *15*, 51–56.